

Two Tricks to Improve Unsupervised Segmentation Learning

Alp Eren Sari¹, Francesco Locatello², and Paolo Favaro¹

¹ University of Bern, Switzerland
{alp.sari, paolo.favaro}@unibe.ch

² Institute of Science and Technology Austria, Austria
francesco.locatello@ista.ac.at

Abstract. We present two practical improvement techniques for unsupervised segmentation learning. These techniques address limitations in the resolution and accuracy of predicted segmentation maps of recent state-of-the-art methods. Firstly, we leverage image post-processing techniques such as guided filtering to refine the output masks, improving accuracy while avoiding substantial computational costs. Secondly, we introduce a multi-scale consistency criterion, based on a teacher-student training scheme. This criterion matches segmentation masks predicted from regions of the input image extracted at different resolutions to each other. Experimental results on several benchmarks used in unsupervised segmentation learning demonstrate the effectiveness of our proposed techniques.

Keywords: Unsupervised · Segmentation · Self-Supervised

1 Introduction

The task of segmenting objects in images is a fundamental first step in extracting semantic information. Current approaches [16, 17] have reached remarkable performance and capabilities by combining various annotation modalities (text, points, bounding boxes, and segmentation masks) and by scaling the training to large datasets. However, recently, several methods [3, 12, 23, 25, 34, 37] have shown that it is possible to learn to segment objects in an unsupervised manner, *i.e.*, without the guidance of any human annotation. Besides the intrinsic scientific significance of such unsupervised learning methods, their main advantage is that they could potentially be scaled to extremely large datasets and across multiple imaging modalities with limited human effort.

Despite encouraging results, these methods seem to be either limited in resolution [23] or to rely on difficult training schemes [3]. Since many of the existing methods [21, 23, 34] rely on DINO features [5], which reduce the initial image resolution by a factor of 8 or 16, we introduce two rather general “tricks” to enhance the resolution of predicted segmentation maps and demonstrate their capabilities on the recent state of the art method *Sempart* for unsupervised segmentation learning [23].³

³ <https://github.com/alpErenSari/segmentation-tricks>

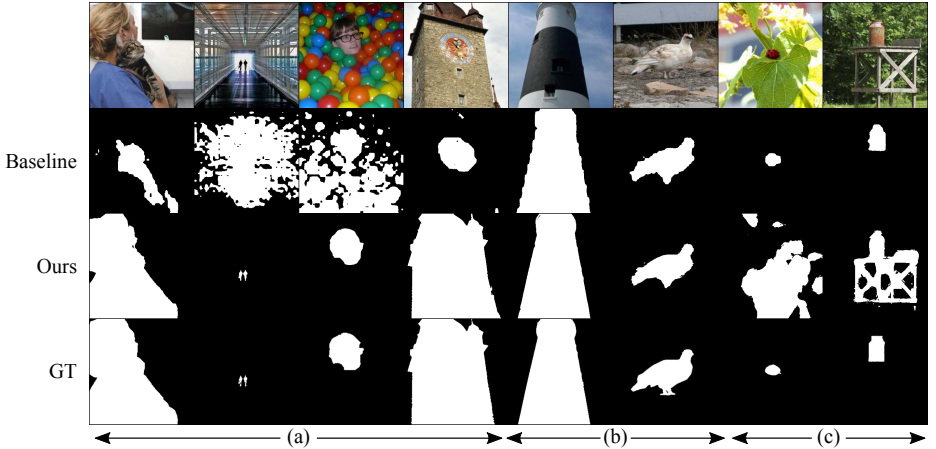


Fig. 1: A qualitative comparison between the baseline and the improved segmentation with the tricks we propose (Ours). The first row shows images sampled from DUTS-TE [33], the second row shows the baseline segmentation predictions, the third row shows the segmentation results with our tricks, and the last row shows the ground truth segmentation masks. In (a) we show 4 image samples where we achieve a significant improvement over the baseline; in (b) we show two image samples where we achieve the same results as in the baseline; in (c) we show two image samples where the tricks make the segmentation masks worse (relative to the ground truth mask). We point out that some of the incorrect masks may also be due to the inherent ambiguity of the unsupervised segmentation task.

A relatively naive attempt to enhance the resolution of the predicted segmentation masks is to simply compute higher-resolution DINO features and then plug them in the affinity matrix used in normalized cuts [23]. However, this immediately comes at a substantial computational cost (the complexity of normalized cuts scales cubically with the size of the affinity matrix) and thus quickly becomes numerically unfeasible.

As mentioned earlier on, we introduce two practical tricks. Our first trick is to use post-processing to enhance the resolution of the output masks. We show that well-established image processing methods such as guided filtering [15] can easily improve the accuracy of the predicted segmentation masks when the input image luminance is used as the filter guidance. Our second trick is a general criterion to enhance the resolution of dense predictions. We introduce a *multi-scale consistency* criterion on the predicted segmentation mask. We do so by using a teacher-student training scheme, where the teacher network takes a zoomed-in region of an image as input and the student network takes the whole image as input. Then, we zoom in on the same region of the predicted segmentation mask from the student network’s prediction and match it to the prediction from the teacher. Because we use the output of the teacher network as a target, we only backpropagate through the student network. A qualitative comparison between the baseline and our method can be seen in Fig. 1.

In summary, our contributions are

- We achieve new state-of-the-art (SotA) results in unsupervised saliency segmentation on the DUT-OMRON [36], DUTS-TE [33], and ECSSD [27] datasets;
- We introduce two novel and general techniques to enhance the resolution of the segmentation masks predicted by existing SotA that are computationally efficient;
- Our techniques are easy to apply and have been thoroughly tested on several benchmarks and in combination with different methods; the code will be made available upon publication.

2 Related Work

Segmentation learning is a task with a long history in computer vision. Some of the classic methods (*e.g.*, normalized cuts) find their way back into the training of deep neural networks [23]. Therefore, we revise some of these basic techniques, give a brief overview of supervised methods, and finally delve deeper into the unsupervised learning methods that relate the most to our techniques.

Spectral Methods. Graph representations are commonly utilized in computer vision and computer graphics for partitioning problems. [26] propose the *normalized cuts* method for image segmentation to handle the bias towards small-isolated segments in the minimum graph cut method [35].

Supervised Image Segmentation. Supervised segmentation methods have been developed on a variety of deep architectures [6, 8, 22, 24] and have recently demonstrated astonishing performance [16, 17]. However, because supervision requires lots of human labor to obtain accurate segmentation masks, these methods face remarkable challenges when they have to be scaled to large datasets.

Self-supervised representations (SSL). The idea of training deep networks without any supervision to obtain effective image representations gained popularity with the success of [4, 5, 7, 13, 14]. In particular, DINO [5] features based on ViT [9] demonstrate capabilities beyond image classification. As discussed in the next paragraph, recent methods for unsupervised segmentation learning find substantial gains by incorporating these SSL features.

Unsupervised Semantic Segmentation. Several recent approaches, such as [21, 29, 34], explore the use of DINO features and graph cuts for semantically meaningful image segmentation. However, these methods often exhibit high computational complexity and relatively low segmentation accuracy. In contrast, [2, 3] rely on the local “shiftability” of segmented objects, but face challenges due to the complexity of their adversarial training schemes. [20] explores pre-trained generative adversarial networks (GAN). However, it is also challenging to generalize this approach due to the limitations of existing GANs. Other methods, like [23, 28, 30, 31], leverage various strategies, such as push-pull forces between pixels, and pseudo-masks, to distill segmentation networks. However, these approaches often suffer from low-resolution image features, limiting the quality of the generated masks.

In this work, we extend the capabilities of Sempart [23], leveraging its recent advancements as the state-of-the-art (SotA) method in unsupervised segmentation learning. Despite its strengths, Sempart encounters limitations in resolution, primarily stemming from its reliance on low-resolution self-supervised learning (SSL) features for feedback. Our proposed tricks address this challenge in a practical and effective manner. These tricks are rather general and can be applied to other methods where an increase in resolution and accuracy is beneficial.

3 Background

In this section we briefly revise some basic definitions to make the paper self-contained and also to provide a context for our proposed techniques.

Normalized Cuts. Normalized cuts [26] is a method to partition a weighted undirected graph $G = (V, E)$ with weights w_{ij} representing the similarity between nodes v_i and v_j , into partitions A and B by minimizing the following loss

$$\text{Ncut}(A, B) = \frac{\text{cut}(A, B)}{\text{assoc}(A, V)} + \frac{\text{cut}(B, A)}{\text{assoc}(B, V)}, \quad (1)$$

$$\text{where } \text{cut}(A, B) \doteq \sum_{u \in A, v \in B} w_{uv} \quad \text{and} \quad \text{assoc}(A, V) \doteq \sum_{u \in A, t \in V} w_{ut}.$$

$\text{cut}(B, A)$, and $\text{assoc}(B, V)$ are also defined similarly. By minimizing Ncut with respect to A and B , the connectivity between partitions A and B is minimized and the connectivity within the partitions is maximized. The weights are collected in an *affinity matrix* W such that its i, j -th entry $W_{i,j} = w_{ij}$. The minimization of normalized cuts loss is NP-complete; hence, [26] proposed a relaxation of the proposed loss which leads to a generalized eigenvalue problem.

TokenCut. [5] shows that the attention maps in DINO strongly relate to the location and shape of the object present in the input image. Thus, TokenCut [34] proposes to utilize DINO features for semantic segmentation combined with normalized cuts as a *post-processing* step. TokenCut [34] minimizes the normalized cuts' loss with the following affinity matrix

$$w_{ij} = \begin{cases} 1 & | \langle F_{v_i}, F_{v_j} \rangle > \tau \\ \epsilon & | \text{otherwise.} \end{cases} \quad (2)$$

where F_{v_i} is the DINO feature corresponding to the node v_i , and τ and ϵ are scalar thresholds to be tuned.

Sempart. Sempart [23] instead leverages DINO features by training a convolutional neural networks (CNN) segmentation head to minimize a loss based on the normalized cut cost. The segmentation head generates two segmentation predictions: one, $S_{\text{coarse}} \in [0, 1]^{|V|}$, at a low-resolution and one, $S_{\text{fine}} \in [0, 1]^{HW}$, at high-resolution, where $|V|$ is the number of DINO features, and H and W are the height and width of the input image. S_{coarse} minimizes the following

variation of the normalized cuts’ loss

$$\mathcal{L}_{\text{Ncut}} = \text{Ncut}(A, B) = \frac{S^T W (1 - S)}{S^T W \mathbf{1}} + \frac{(1 - S)^T W S}{(1 - S)^T W \mathbf{1}}, \quad (3)$$

where $\mathbf{1}$ is a vector of ones. Eq. (3) is optimized only with respect to the low resolution mask S_{coarse} . High-resolution mask S_{fine} is guided through a consistency loss

$$\mathcal{L}_{\text{SR}} = \|\text{down}(S_{\text{fine}}) - S_{\text{coarse}}\|_2^2, \quad (4)$$

which matches the downsampled S_{fine} and S_{coarse} , and $\mathcal{L}_{\text{GTV-fine}}$ is a graph total variation (GTV) loss that works on the high-resolution mask. An additional GTV loss $\mathcal{L}_{\text{GTV-coarse}}$ computed with S_{coarse} is also used for additional guidance. $\mathcal{L}_{\text{GTV-fine}}$ and $\mathcal{L}_{\text{GTV-coarse}}$ are given as

$$\mathcal{L}_{\text{GTV-fine/coarse}} = \frac{1}{2} \sum_{(i,j) \in E} a_{ij} (s_i - s_j)^2, \quad (5)$$

$$a_{ij}^{\text{fine}} = \exp(-\|x_i - x_j\|_2^2 / \sigma), \quad (6)$$

$$a_{ij}^{\text{coarse}} = w_{ij} \mathbf{I}\{i \in \mathcal{N}(j)\}, \quad (7)$$

where $\mathcal{N}(j)$ is set of nodes adjacent to node j , and \mathbf{I} is the indicator function. The only difference between $\mathcal{L}_{\text{GTV-fine}}$ and $\mathcal{L}_{\text{GTV-coarse}}$ is that x_i is a pixel value from the input image for fine GTV, but it is the DINO feature for the coarse GTV. Finally, the segmentation head is trained with the combined loss

$$\mathcal{L}_{\text{sempart}} = \mathcal{L}_{\text{Ncut}} + \lambda_{\text{GTV-coarse}} \mathcal{L}_{\text{GTV-coarse}} + \lambda_{\text{GTV-fine}} \mathcal{L}_{\text{GTV-fine}} + \lambda_{\text{SR}} \mathcal{L}_{\text{SR}}. \quad (8)$$

4 Two Tricks

Recent unsupervised segmentation methods face diverse challenges, such as low-resolution feedback [21, 23, 34], instability during training due to the incorporation of adversarial losses [2, 3, 20], and misalignment between the predicted mask edges with the actual object edges. Many methods attempt to address the latter by employing bilateral filtering [1] as a post-processing step, though this approach has shown performance degradation in certain instances, as in [3, 23]. To tackle this issue, we propose to use guided filtering [15] as an alternative post-processing step, which has not been explored extensively in recent literature. Our experiments in Sec. 5 demonstrate that guided filtering significantly improves segmentation performance across various unsupervised methods.

The second trick we propose aims to mitigate the challenges associated with low-resolution feedback in methods incorporating SSL features. We introduce an equivariance loss based on random cropping of the input image and mask prediction in a teacher-student training scheme. The primary motivation behind this approach is to derive a finely detailed segmentation mask from a cropped and zoomed-in image, encouraging the student network to generate a matching



Fig. 2: Some sampled images from DUTS-TE [33] containing small or intricate objects, which are challenging for segmentation tasks.

prediction for the original image. We use the same networks as the student and the teacher. This process is illustrated in Fig. 3.

Guided Filtering. The guided filter [15] is a member of the edge-preserving smoothing image filter family. Although bilateral filtering [1] is commonly used in segmentation applications, we consider guided filtering because of two essential advantages compared to bilateral filtering: a lower computational complexity and no gradient reversal effects.

The guided filter is a locally linear filter with the hypothesis that the output image is an affine transformation of the input and this affine transformation is constant within a local window. Hence, the input and output pixel values can be expressed as $q_i = a_k I_i + b_k = p_i - n_i, \forall i \in \omega_k$, where the q_i is the output image, p_i is the input image, n_i is the estimated noise, I_i is the guidance image, a_k and b_k are the affine transformation parameters, and ω_k is the local window. To estimate the parameters a_k and b_k the loss $E(a_k, b_k) = \sum_{i \in \omega_k} ((a_k I_i + b_k - p_i)^2 + \epsilon a_k^2)$ is minimized for all local windows ω_k . After taking the derivative of the loss, and equating it to 0, we get $a_k = (\frac{1}{|\omega|} \sum_{i \in \omega_k} I_i p_i - \mu_k \bar{p}_k) / (\sigma_k^2 + \epsilon)$ and $b_k = \bar{p}_k - a_k \mu_k$. We will denote the guided filtering process as $\text{GF}(\cdot, \cdot)$ in the rest of the paper. For instance, $q = \text{GF}(p, I)$ means that the image p is filtered with the image I 's guidance, and we obtain q as the filtered image.

We propose to set p as the predicted segmentation mask and I as the luminance of the input image. In other words, we apply guided filtering on the

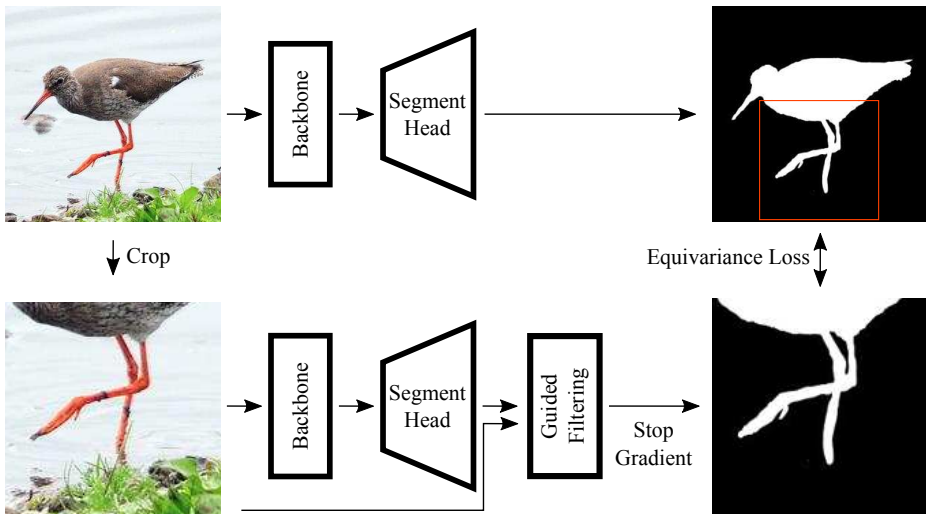


Fig. 3: The illustration of the proposed multi-scale consistency procedure. First, we predict a segmentation from an input image. Then, we randomly crop a portion of the input image, predict a more detailed segmentation mask, refine this prediction with guided filtering, and apply a stop-gradient operation to the final mask to prevent a mask prediction collapse. Finally, we calculate the mean squared error between the corresponding region of the initial mask and the detailed target mask.

predicted mask with the guidance of the grayscale version of the input image. Since guided filtering is essentially an affine transformation, the gradients of the filtered image and the guidance image will be proportional, which can be regarded as the alignment of the input image edges according to the guidance from the image edges. **Multi-Scale Consistency.** One challenge associated with incorporating a segmentation head over a ViT [9] feature map (as with DINO) is the loss of details, particularly for small objects or structures within the image. Sempart [23] addresses this issue by feeding the input image into the segmentation head and by applying a total variation loss on the resulting high-resolution mask. Despite these efforts, the model suffers from inaccurate segmentations of small objects or of objects with thin structures, as illustrated in Fig. 2. We aim to tackle this problem by introducing an equivariance loss based on random cropping. Whereas Leopart [39] previously proposed a similar concept for training self-supervised image representations, we extend this idea by directly applying the equivariance loss to the segmentation prediction, as depicted in Fig. 3. The proposed equivariance loss is computed through the following steps:

1. Given an input image and a segmentation framework denoted as I and $f(\cdot)$ respectively, predict a mask denoted as \hat{s} . This process can be expressed as $f(I) = \hat{s}$.
2. Randomly crop the same region of the input image and the predicted mask and enlarge both of them to the original input image size. This operation on

Table 1: The unsupervised saliency segmentation results on DUT-OMRON [36], DUTS-TE [33], and ECSSD [27]. The best results are indicated in **bold**. Sempart* indicates our implementation of Sempart [23] since the code is currently unavailable. ‘‘Ours’’ indicates the application of the proposed trick over the Sempart baseline. We demonstrate improvements over the baseline implementation we have.

Model	DUT-OMRON [36]			DUTS-TE [33]			ECSSD [27]		
	Acc	IoU	$maxF_\beta$	Acc	IoU	$maxF_\beta$	Acc	IoU	$maxF_\beta$
LOST [29]	.797	.410	.473	.871	.518	.611	.895	.654	.758
TokenCut [34]	.880	.533	.600	.903	.576	.672	.918	.712	.803
FOUND [30] - single	.920	.586	.683	.939	.637	.733	.912	.793	.946
MOVE [3]	.923	.615	.712	.950	.713	.815	.954	.830	.916
Sempart [23]	.932	.668	.764	.959	.749	.867	.964	.855	.947
Sempart*	.908	.664	.758	.949	.761	.856	.950	.853	.925
Ours	.920	.684	.765	.956	.787	.869	.952	.862	.931
MOVE [3] + BF	.931	.636	.734	.951	.687	.821	.953	.801	.916
Sempart + BF	.942	.698	.799	.958	.749	.879	.963	.850	.944
Sempart* + BF	.914	.689	.770	.950	.765	.857	.950	.849	.925
Ours + BF	.920	.675	.763	.950	.742	.855	.945	.830	.920
SELFMask w/ MOVE	.933	.666	.756	.954	.728	.829	.956	.835	.921
SELFMask w/ Sempart	.942	.698	.799	.958	.749	.879	.963	.850	.944
SELFMask w/ Sempart*	.923	.674	.768	.953	.743	.866	.962	.854	.942
SELFMask w/ Ours	.935	.685	.790	.956	.747	.881	.962	.852	.948

I , \hat{s} can be expressed as $CU(I, \hat{s}) = \{I_c, s_c\}$ where $CU(\cdot, \cdot)$, I_c , and s_c are the crop-zoom function, the resultant image and mask.

- Use the resultant image to predict a mask and refine this mask with guided image filtering, which can be expressed as $f(I_c) = \hat{s}_c$.
- Apply stop gradient afterwards to prevent a collapse of the predicted masks, which we denote as $SG[GF(\hat{s}_c)] = s_{target}$, where s_{target} is the final target for our loss, and $SG[\cdot]$ is the stop gradient operation.
- Calculate the mean squared error between the new prediction and the corresponding region of the first segmentation prediction as $\mathcal{L}_{eq} = \frac{1}{hw} \|s_c - s_{target}\|_2^2$ where h and w are the height and width of the corresponding masks \hat{s}_c and s_{target} .

In our experiments, we added \mathcal{L}_{eq} multiplied with the parameter λ_{eq} to the overall loss (8). We also used the cropped image to train the network.

5 Experimental Results

We evaluate the tricks we propose on Sempart [23] since it is the current state-of-the-art unsupervised segmentation learning method, it trains stably, and it converges quickly. The evaluations are performed for saliency segmentation and single object detection since Sempart [23] and previous works were evaluated

on these tasks. All the evaluations were performed using the fine branch of Sempart [23]. The improved baseline with the proposed tricks is denoted as “ours”.

5.1 Implementation

Since the code of Sempart [23] has not been released yet, we implemented it by following the implementation details in the paper with minor changes. The Sempart [23] results obtained with our implementation are denoted as “Sempart^{**}”⁴ **Sempart.** We utilize the ViT-s/8 version of the official DINO [5], set input image size to 320×320 , extract the keys from the last layer with size $384 \times 40 \times 40$, and use them to perform segmentation and compute the normalized cut loss. AdamW [19] is utilized for optimization with a learning rate of 1×10^{-4} , $\beta = (0.9, 0.99)$, and *weight_decay* of 0. Everything was implemented in Pytorch and trained for 30 epochs on a single NVIDIA GTX 3090 GPU with a batch size of 8. We set $\lambda_{SR} = 1$, $\lambda_{GTV-coarse} = 1$, $\lambda_{GTV-fine} = 1$, $\lambda_{Ncut-Crop} = 0.01$, and $\lambda_{eq} = 0.01$ where $\lambda_{Ncut-Crop}$ is the normalized cut loss calculated on the random cropped and upsampled image region. For graph total variation losses, the average of each pixel’s loss was used instead of the summation, since we observed that this improves stability.

Data augmentation. The shorter dimension (width or height) of the input images are first resized to 355, and a random 320×320 region is cropped. We also used slight color jittering and random grayscale with a probability of 0.2.

Graph affinity. Contrary to Sempart [23], we use keys from the last layer of ViT-S/8 DINO, and set $\tau = 0.4$ and $\epsilon = 1 \times 10^{-6}$. These changes were made since our implementation following the exact settings of Sempart failed to converge. We keep the hyper-parameters for $\mathcal{L}_{GTV-coarse}$ and $\mathcal{L}_{GTV-fine}$ same.

Foreground selection. During the evaluation, we calculate the average over all pixels in a batch, and we invert the masks if this mean is greater than 0.5. The assumption is that the foreground should cover a smaller area than the background on average.

Multi-scale consistency. We randomly crop the same 80×80 fraction of the input image and the mask prediction. Afterward, these crops are upscaled to 320×320 . We also used the random cropped image to train the Sempart [23].

Guided filtering. To apply guided filtering on segmentation predictions, initially, we re-scale the pixel values of the guidance image into the range of 0 and 1, just like the mask prediction. Afterward, the pixel values of the guidance image are averaged to get a grayscale estimation of the image. This final one-channel image is utilized for the guided filtering.

5.2 Unsupervised Saliency Segmentation

Datasets. We used the DUTS-TR [33] dataset which contains 10,553 object-centric images for training in every experiment, as [3, 23, 28]. To evaluate the

⁴ The implementation can be found at <https://github.com/alpErenSari/segmentation-tricks>

performance of unsupervised saliency segmentation, we used DUT-OMRON [36] dataset with 5,168 images, DUTS-TE [33] dataset with 5,019 images, and ECSSD [27] dataset with 1,000 images.

Evaluation. Three metrics are reported in our work as [3, 23, 28], which are pixel mask accuracy (Acc), intersection over union (IoU), and max F_β [34]. Accuracy is the percentage of pixels classified accurately, and intersection over union (IoU) is the ratio between intersection and union of the predicted and ground-truth segmentation masks, and

$$F_\beta = \frac{(1 + \beta^2) \times \text{Precision} \times \text{Recall}}{\beta^2 \times \text{Precision} + \text{Recall}}, \quad (9)$$

with $\beta = 0.3$.

Results. In Tab. 1, we present a comprehensive comparison of our results with the recent state-of-the-art method Sempart [23]. Our implementation, denoted as ‘‘Sempart*’’, undergoes evaluation across three distinct criteria: baseline results, post-processed baseline results employing bilateral filtering [1], and outcomes derived from SELFMASK [28], trained with pseudo-masks generated by various methods. The comparison reveals the efficacy of our approach in advancing unsupervised saliency segmentation.

Our results show state-of-the-art Intersection over Union (IoU) performance across all three datasets. Additionally, our approach achieves the best max F_β scores on DUT-OMRON [36] and DUTS-TE [33] datasets. Notably, with the help of the proposed tricks, we consistently outperform the baseline model across all evaluation scenarios, displaying their effectiveness.

When considering the notable gaps between our implemented baseline and the reported baseline, particularly in terms of accuracy (Acc) and max F_β metrics, it becomes evident that our approach has the potential to establish a new state-of-the-art benchmark with precisely the same baseline. This observation reinforces the significance of our proposed techniques in pushing the boundaries of unsupervised saliency segmentation performance.

5.3 Single Object Detection

Datasets. The evaluation of single object detection was done on three datasets, which are the train split of COCO20K [18], the training and validation splits of Pascal VOC07 [10], and Pascal VOC12 [11].

Evaluation. First, the predicted mask is split into parts if it’s not fully connected. Then, we select the mask with the largest bounding box as our object prediction and calculate the IoU between our prediction and the ground-truth bounding box. Finally, the percentage of the IoUs higher than 0.5 is calculated, which is known as the *Correct Localization* (CorLoc) metric.

Results. In Tab. 2, we conduct a comprehensive comparison between our results and the recent state-of-the-art MOVE [3], as well as our baseline in object detection. Our tricks significantly enhance the baseline across all three datasets considered. This improvement is evident in detection accuracy, underscoring the effectiveness of our approach in advancing unsupervised object detection.

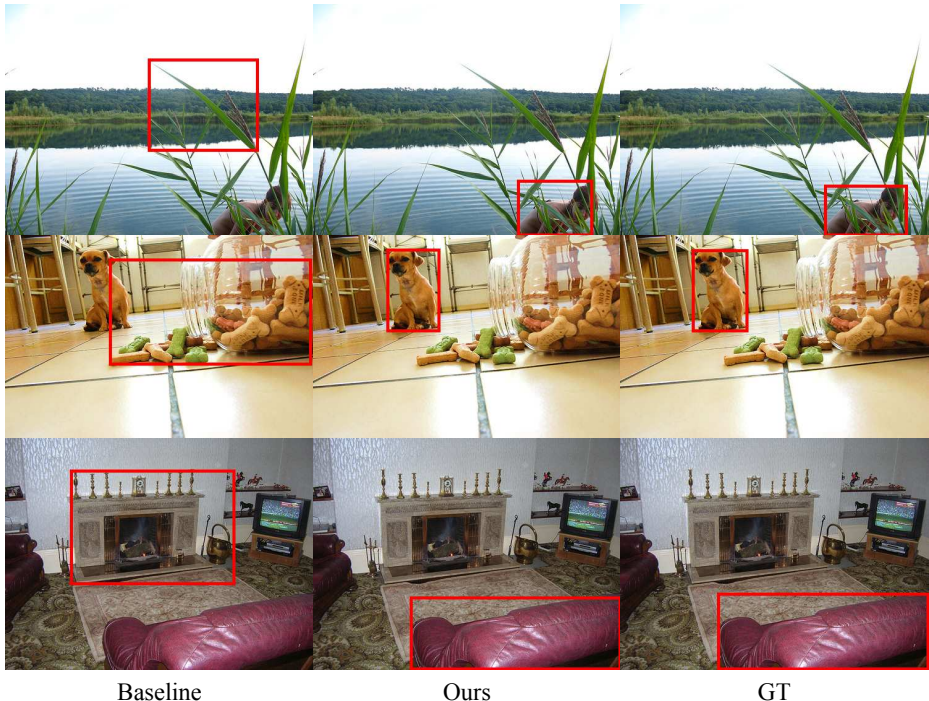


Fig. 4: Some examples cases from Pascal VOC12 [11] where our tricks improve object detection over baseline.

The observed disparities between the reported baseline and our implemented version prompts the assertion that our approach has the potential to establish a new state-of-the-art benchmark in both Pascal VOC07 [10] and COCO20K [18] datasets. This claim is substantiated by the consistent and noteworthy improvements achieved across various evaluation metrics.

Our ablation study in Sec. 5.4 provides additional insights, revealing that random cropping emerges as a key contributor to the overall improvement in object detection. Specifically, Fig. 4 visually depicts how random cropping facilitates the detection of small objects and, in some instances, objects with occlusion. This emphasizes the nuanced impact of each proposed technique, with random cropping playing a pivotal role in enhancing the model’s capability to handle challenging detection scenarios.

5.4 Ablations

We conducted various ablation experiments to demonstrate the effectiveness of the proposed enhancements. These experiments involved evaluating the impact of the proposed techniques compared to the baseline in unsupervised saliency segmentation and single object detection. Additionally, we performed an ablation

Table 2: Comparison of single object detection on Pascal VOC07 [10], Pascal VOC12 [11], COCO20K [18] with CorLoc metric. The best results are indicated in **bold**. Sempart* indicates our implementation of Sempart [23]. ($\uparrow z$) indicate the improvements over the baseline.

Model	VOC07 [10]	VOC12 [11]	COCO20K [18]
LOST [29]	61.9	64.0	50.7
Deep Spectral [21]	62.7	66.4	50.7
TokenCut [34]	68.8	72.1	58.8
MOVE [3]	76.0	78.8	66.6
Sempart [23]	75.1	76.8	66.4
Sempart*	71.7	75.9	61.3
Ours	74.4 ($\uparrow 2.7$)	77.0 ($\uparrow 1.1$)	63.4 ($\uparrow 2.1$)

study on the guided filtering, comparing its performance with recent methods such as TokenCut [34] and MOVE [3] in unsupervised saliency segmentation. For the saliency segmentation ablation, we trained different baselines using various SSL backbones and demonstrated that our techniques consistently outperformed the baselines across different backbones.

The tricks on saliency segmentation. In Tab. 3, we present the Intersection over Union (IoU) results obtained from the evaluation of unsupervised saliency segmentation on three datasets: DUT-OMRON [36], DUTS-TE [33], and ECSSD [27]. The original baseline is trained with DINO [5] ViT-S/8 as the backbone. Additionally, we provide results for baselines trained with DINO ViT-S/16 and IBOT [38] ViT-S/16 as the backbones. Our findings indicate that across different backbones, the proposed techniques significantly enhance segmentation performance. Notably, guided filtering emerges as a key contributor to the improved segmentation results.

The tricks on single object detection. In Tab. 4, we demonstrate the enhancement achieved by our techniques in object detection based on the CorLoc metric. The evaluation is performed on datasets comprising the train and validation splits of Pascal VOC07 [10] and Pascal VOC12 [11], as well as the train split of COCO20K [18]. Notably, unlike the case of saliency segmentation, we observe that random cropping yields the most significant improvement in object detection performance.

Guided filtering with different methods. In Tab. 5, our findings indicate that the application of guided filtering significantly enhances the performance of recent saliency segmentation methods TokenCut [34] and MOVE [3]. We present results Acc, IoU, and the $maxF_\beta$ metric across evaluation datasets including DUT-OMRON [36], DUTS-TE [33], and ECSSD [27]. Comparative analysis with baseline methods, incorporating bilateral filtering [1], is also included. Notably, the results in Tab. 5 demonstrate consistent improvement in all metrics with guided filtering, which contrasts with the performance of bilateral filtering.

Table 3: The ablations on unsupervised saliency segmentation with mIoU on three datasets; DUT-OMRON [36], DUTS-TE [33], and ECSSD [27]. The best results are indicated with **bold**.

Backbone	Crop	GF	DUT-OMRON [36]	DUTS-TE [33]	ECSSD [27]
DINO [5] ViT-S/8	×	×	.664	.761	.853
	✓	×	.670	.772	.852
	×	✓	.684	.784	.869
	✓	✓	.684	.787	.862
DINO [5] ViT-S/16	×	×	.604	.692	.784
	✓	×	.647	.710	.812
	×	✓	.608	.697	.788
	✓	✓	.652	.714	.816
IBOT [38] ViT-S/16	×	×	.584	.650	.793
	✓	×	.588	.654	.797
	×	✓	.600	.664	.806
	✓	✓	.604	.668	.811

Table 4: The ablations on unsupervised single object detection with CorLoc on three datasets; Pascal VOC07 [10], Pascal VOC12 [11], COCO20K [18]. The best results are indicated with **bold**.

Crop	GF	VOC07 [10]	VOC12 [11]	COCO20K [18]
×	×	71.7	75.9	61.3
✓	×	74.2	77.0	64.3
×	✓	71.7	75.7	61.3
✓	✓	74.4	77.0	63.4

5.5 Limitations and Potential Negative Impacts

Limitations. Our method exhibits challenges in scenarios where saliency within an image is unambiguous or when multiple objects are present in the scene. Some visual examples can be seen in Fig. 5, where our method tends to segment all objects in the scene, whereas human annotators are inclined to select smaller and easily movable objects. This discrepancy highlights a limitation in our model’s ability to prioritize and differentiate between objects based on their perceived saliency. Moreover, in instances where the salient object and the background share visual similarities our method encounters difficulty, making it challenging to distinguish between them accurately. This issue is particularly pronounced when the visual features of the salient and background objects closely resemble each other. The struggle to discern between these visually similar elements contributes to inaccuracies in segmentation, as depicted in various scenarios.

Potential negative impacts. Our method is unlikely to have negative impacts, as its primary function is segmenting objects in images, which can be

Table 5: The ablations of guided filtering [15] and bilateral filtering [1] with TokenCut [34] and MOVE [3] on unsupervised saliency segmentation with same datasets and metrics in Tab. 1. The best results for each method are indicated with **bold**.

Model	DUT-OMRON [36]			DUTS-TE [33]			ECSSD [27]		
	Acc	IoU	$maxF_{\beta}$	Acc	IoU	$maxF_{\beta}$	Acc	IoU	$maxF_{\beta}$
TokenCut	.880	.533	.600	.903	.576	.672	.918	.712	.803
TokenCut + GF	.880	.553	.676	.907	.597	.740	.925	.740	.861
TokenCut + BF	.897	.618	.697	.914	.624	.755	.934	.772	.874
MOVE	.923	.615	.712	.950	.713	.815	.954	.830	.916
MOVE + GF	.925	.615	.631	.952	.726	.813	.958	.843	.923
MOVE + BF	.931	.636	.734	.951	.687	.821	.953	.801	.916



Fig. 5: Some of the failure cases of our method from DUTS-TE [33]. In most cases the saliency is unambiguous or the background and the foreground are almost indistinguishable.

accomplished by alternative methods or through manual annotation by humans.

6 Conclusion

We introduced two tricks that can be flexibly incorporated into unsupervised image segmentation. We demonstrated their effectiveness with state-of-the-art results on unsupervised saliency segmentation tasks, combined with the recent state-of-the-art baseline. Moreover, we demonstrated these two tricks can be effective even if the baseline was trained with different backbones and combined with other recent methods.

References

1. Barron, J.T., Poole, B.: The fast bilateral solver. In: ECCV. pp. 617–632. Springer (2016) [5](#), [6](#), [10](#), [12](#), [14](#)
2. Bielski, A., Favaro, P.: Emergence of object segmentation in perturbed generative models. *NeurIPS* **32** (2019) [3](#), [5](#)
3. Bielski, A., Favaro, P.: Move: Unsupervised movable object segmentation and detection. *NeurIPS* **35**, 33371–33386 (2022) [1](#), [3](#), [5](#), [8](#), [9](#), [10](#), [12](#), [14](#)
4. Caron, M., Misra, I., Mairal, J., Goyal, P., Bojanowski, P., Joulin, A.: Unsupervised learning of visual features by contrasting cluster assignments. *NeurIPS* **33**, 9912–9924 (2020) [3](#)
5. Caron, M., Touvron, H., Misra, I., Jégou, H., Mairal, J., Bojanowski, P., Joulin, A.: Emerging properties in self-supervised vision transformers. In: ICCV. pp. 9650–9660 (2021) [1](#), [3](#), [4](#), [9](#), [12](#), [13](#), [17](#)
6. Chen, L.C., Papandreou, G., Schroff, F., Adam, H.: Rethinking atrous convolution for semantic image segmentation. arXiv preprint arXiv:1706.05587 (2017) [3](#)
7. Chen, T., Kornblith, S., Norouzi, M., Hinton, G.: A simple framework for contrastive learning of visual representations. In: ICML. pp. 1597–1607. PMLR (2020) [3](#)
8. Cheng, B., Schwing, A., Kirillov, A.: Per-pixel classification is not all you need for semantic segmentation. *NeurIPS* **34**, 17864–17875 (2021) [3](#)
9. Dosovitskiy, A., Beyer, L., Kolesnikov, A., Weissenborn, D., Zhai, X., Unterthiner, T., Dehghani, M., Minderer, M., Heigold, G., Gelly, S., et al.: An image is worth 16x16 words: Transformers for image recognition at scale. In: ICLR (2020) [3](#), [7](#)
10. Everingham, M., Van Gool, L., Williams, C.K., Winn, J., Zisserman, A.: The pascal visual object classes (voc) challenge. *IJCV* **88**, 303–338 (2010) [10](#), [11](#), [12](#), [13](#)
11. Everingham, M., Winn, J.: The pascal visual object classes challenge 2012 (voc2012) development kit. *Pattern Anal. Stat. Model. Comput. Learn., Tech. Rep* **2007**(1-45), 5 (2012) [10](#), [11](#), [12](#), [13](#)
12. Hamilton, M., Zhang, Z., Hariharan, B., Snavely, N., Freeman, W.T.: Unsupervised semantic segmentation by distilling feature correspondences. In: ICLR (2021) [1](#)
13. He, K., Chen, X., Xie, S., Li, Y., Dollár, P., Girshick, R.: Masked autoencoders are scalable vision learners. In: CVPR. pp. 16000–16009 (2022) [3](#)
14. He, K., Fan, H., Wu, Y., Xie, S., Girshick, R.: Momentum contrast for unsupervised visual representation learning. In: CVPR. pp. 9729–9738 (2020) [3](#)
15. He, K., Sun, J., Tang, X.: Guided image filtering. *IEEE TPAMI* **35**(6), 1397–1409 (2012) [2](#), [5](#), [6](#), [14](#), [17](#)
16. Ke, L., Ye, M., Danelljan, M., Tai, Y.W., Tang, C.K., Yu, F., et al.: Segment anything in high quality. *NeurIPS* **36** (2024) [1](#), [3](#)
17. Kirillov, A., Mintun, E., Ravi, N., Mao, H., Rolland, C., Gustafson, L., Xiao, T., Whitehead, S., Berg, A.C., Lo, W.Y., et al.: Segment anything. arXiv preprint arXiv:2304.02643 (2023) [1](#), [3](#)
18. Lin, T.Y., Maire, M., Belongie, S., Hays, J., Perona, P., Ramanan, D., Dollár, P., Zitnick, C.L.: Microsoft coco: Common objects in context. In: ECCV. pp. 740–755. Springer (2014) [10](#), [11](#), [12](#), [13](#)
19. Loshchilov, I., Hutter, F.: Decoupled weight decay regularization. In: ICLR (2018) [9](#)
20. Melas-Kyriazi, L., Rupprecht, C., Laina, I., Vedaldi, A.: Finding an unsupervised image segmenter in each of your deep generative models. In: ICLR (2021) [3](#), [5](#)

21. Melas-Kyriazi, L., Rupprecht, C., Laina, I., Vedaldi, A.: Deep spectral methods: A surprisingly strong baseline for unsupervised semantic segmentation and localization. In: CVPR. pp. 8364–8375 (2022) [1](#), [3](#), [5](#), [12](#)
22. Qin, X., Zhang, Z., Huang, C., Dehghan, M., Zaiane, O.R., Jagersand, M.: U2-net: Going deeper with nested u-structure for salient object detection. PR **106**, 107404 (2020) [3](#)
23. Ravindran, S., Basu, D.: Sempart: Self-supervised multi-resolution partitioning of image semantics. In: ICCV. pp. 723–733 (2023) [1](#), [2](#), [3](#), [4](#), [5](#), [7](#), [8](#), [9](#), [10](#), [12](#), [17](#)
24. Ronneberger, O., Fischer, P., Brox, T.: U-net: Convolutional networks for biomedical image segmentation. In: Medical Image Computing and Computer-Assisted Intervention–MICCAI 2015: 18th International Conference, Munich, Germany, October 5–9, 2015, Proceedings, Part III 18. pp. 234–241. Springer (2015) [3](#)
25. Seitzer, M., Horn, M., Zadaianchuk, A., Zietlow, D., Xiao, T., Simon-Gabriel, C., He, T., Zhang, Z., Schölkopf, B., Brox, T., et al.: Bridging the gap to real-world object-centric learning. In: ICLR (2023) [1](#)
26. Shi, J., Malik, J.: Normalized cuts and image segmentation. IEEE TPAMI **22**(8), 888–905 (2000) [3](#), [4](#)
27. Shi, J., Yan, Q., Xu, L., Jia, J.: Hierarchical image saliency detection on extended cssd. IEEE TPAMI **38**(4), 717–729 (2015) [3](#), [8](#), [10](#), [12](#), [13](#), [14](#), [17](#), [19](#)
28. Shin, G., Albanie, S., Xie, W.: Unsupervised salient object detection with spectral cluster voting. In: CVPR. pp. 3971–3980 (2022) [3](#), [9](#), [10](#)
29. Siméoni, O., Puy, G., Vo, H.V., Roburin, S., Gidaris, S., Bursuc, A., Pérez, P., Marlet, R., Ponce, J.: Localizing objects with self-supervised transformers and no labels. In: BMVC (2021) [3](#), [8](#), [12](#)
30. Siméoni, O., Sekkat, C., Puy, G., Vobecký, A., Zablocki, É., Pérez, P.: Unsupervised object localization: Observing the background to discover objects. In: CVPR. pp. 3176–3186 (2023) [3](#), [8](#)
31. Van Gansbeke, W., Vandenhende, S., Georgoulis, S., Van Gool, L.: Unsupervised semantic segmentation by contrasting object mask proposals. In: ICCV. pp. 10052–10062 (2021) [3](#)
32. Vaswani, A., Shazeer, N., Parmar, N., Uszkoreit, J., Jones, L., Gomez, A.N., Kaiser, Ł., Polosukhin, I.: Attention is all you need. NeurIPS **30** (2017) [17](#)
33. Wang, L., Lu, H., Wang, Y., Feng, M., Wang, D., Yin, B., Ruan, X.: Learning to detect salient objects with image-level supervision. In: CVPR. pp. 136–145 (2017) [2](#), [3](#), [6](#), [8](#), [9](#), [10](#), [12](#), [13](#), [14](#), [17](#), [18](#), [19](#), [20](#), [22](#)
34. Wang, Y., Shen, X., Yuan, Y., Du, Y., Li, M., Hu, S.X., Crowley, J.L., Vaufreydaz, D.: Tokencut: Segmenting objects in images and videos with self-supervised transformer and normalized cut. IEEE TPAMI (2023) [1](#), [3](#), [4](#), [5](#), [8](#), [10](#), [12](#), [14](#)
35. Wu, Z., Leahy, R.: An optimal graph theoretic approach to data clustering: Theory and its application to image segmentation. IEEE TPAMI **15**(11), 1101–1113 (1993) [3](#)
36. Yang, C., Zhang, L., Lu, H., Ruan, X., Yang, M.H.: Saliency detection via graph-based manifold ranking. In: CVPR. pp. 3166–3173 (2013) [3](#), [8](#), [10](#), [12](#), [13](#), [14](#), [17](#), [18](#), [21](#)
37. Zadaianchuk, A., Kleindessner, M., Zhu, Y., Locatello, F., Brox, T.: Unsupervised semantic segmentation with self-supervised object-centric representations. In: ICLR (2022) [1](#)
38. Zhou, J., Wei, C., Wang, H., Shen, W., Xie, C., Yuille, A., Kong, T.: Image bert pre-training with online tokenizer. In: ICLR (2021) [12](#), [13](#)
39. Ziegler, A., Asano, Y.M.: Self-supervised learning of object parts for semantic segmentation. In: CVPR. pp. 14502–14511 (2022) [7](#)

A Implementation Details

We have implemented Sempart [23] using the implementation details provided in their supplementary material. While we made minor adjustments, we preserved the original architecture largely. Specifically, the segmentation head of Sempart utilizes DINO [5] features to generate a low-resolution and a high-resolution segmentation mask.

Low-resolution Mask. To begin, the DINO features $F \in \mathbb{R}^{384}$ are projected to $\tilde{F} \in \mathbb{R}^{64}$. Subsequently, these features get passed through a transformer encoder layer [32] with two attention heads and two layers, resulting in another set of features denoted as $\tilde{F}' \in \mathbb{R}^{64}$. This intermediate feature representation is then processed through a 1×1 convolutional layer followed by a sigmoid layer to produce the low-resolution segmentation prediction. Furthermore, the same feature representation is input to an upsampling layer to obtain the high-resolution segmentation prediction.

High-resolution Mask. We used the same architecture from Sempart. Each upsampling block consists of a 2×2 bilinear upsampling, concatenation with the input image and a conv block. A conv block is a sequence of a 3×3 convolutional layer, batch normalization, and leaky ReLU with a negative slope of 0.01.

To restore the original image resolution, we employed three upsampling blocks, considering the use of DINO ViT-S/8. The final upsampling block comprises two convolutional blocks. Then, the resulting feature is concatenated with the input image. The final high-resolution segmentation is predicted using a 1×1 convolutional layer followed by a sigmoid activation function. Before bilinear sampling, the feature dimensions are 64, 192, and 128. Following concatenation with the input image, the output feature expands to 131 channels.

B Supplementary Experimental Results

B.1 Unsupervised Saliency Segmentation

We conducted a detailed analysis of the Intersection over Union (IoU) across three datasets: DUT-OMRON [36], DUTS-TE [33], and ECSSD [27]. We compared the performance of our baseline model against an improved version incorporating our proposed tricks, as depicted in Fig. 6, Fig. 7, and Fig. 8.

We first computed the ratio of salient objects in each sample and divided the samples into 20 categories concerning their object size. Subsequently, we calculated the average IoU within each category. Our findings revealed that the error distributions exhibited similar patterns in both cases, with a notable concentration of poor predictions observed in samples containing either tiny or huge objects.

Furthermore, we observed that the proposed multi-scale consistency loss and guided filtering techniques [15] significantly improved with extreme cases. Additionally, our improved model consistently outperformed the baseline across all mask sizes, indicating the efficacy of our proposed enhancements.

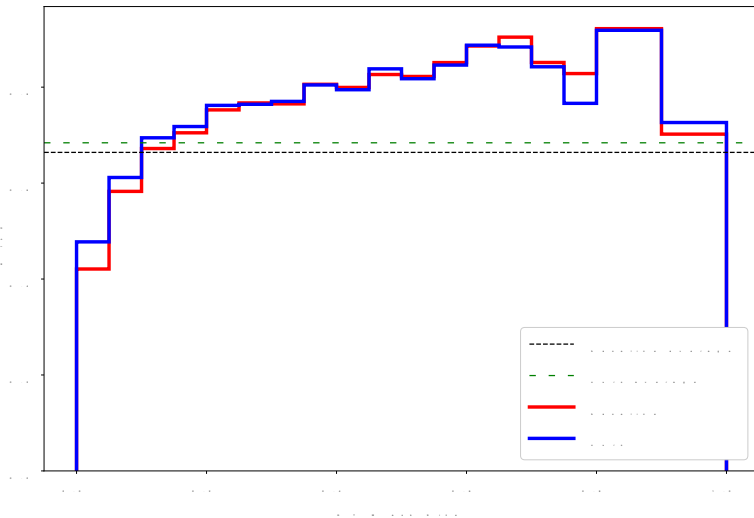


Fig. 6: Distribution of intersection over union to the GT mask size on DUT-OMRON [36]. We divided the samples into 20 categories regarding the GT mask size.

B.2 Quantitative Results

We present more quantitative comparisons of the baseline and our improved version on random samples from DUT-OMRON [36] dataset on Fig. 10, and DUTS-TE [33] dataset on Fig. 9. It’s possible to see that our tricks improve the segmentation in the edge cases where there are huge or tiny objects in the scene, which supports our analysis in Appendix B.1.

B.3 Limitations

Figure 11 presents examples of failed segmentation cases from the DUTS-TE dataset [33]. These instances exhibit challenges such as ambiguous ground-truth (GT) masks or scenes with multiple objects that require segmentation. Particularly, the failed cases often involve smaller objects in the GT annotations, aligning with the observations discussed in subsection B.1.

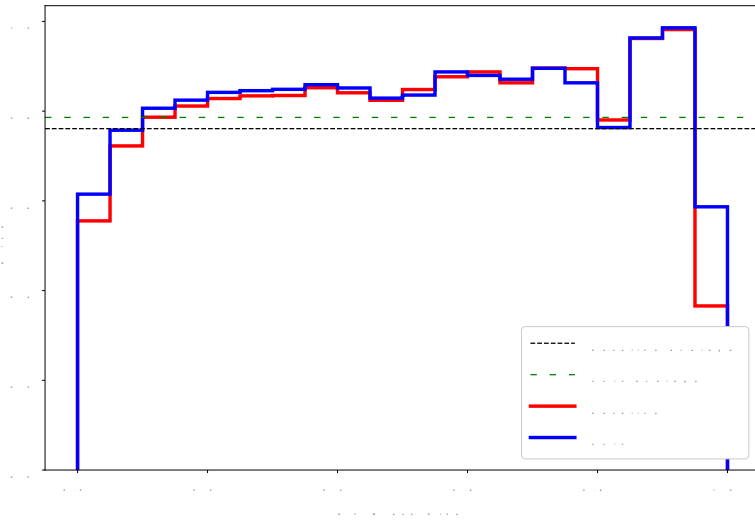


Fig. 7: Distribution of intersection over union to the GT mask size on DUTS-TE [33].

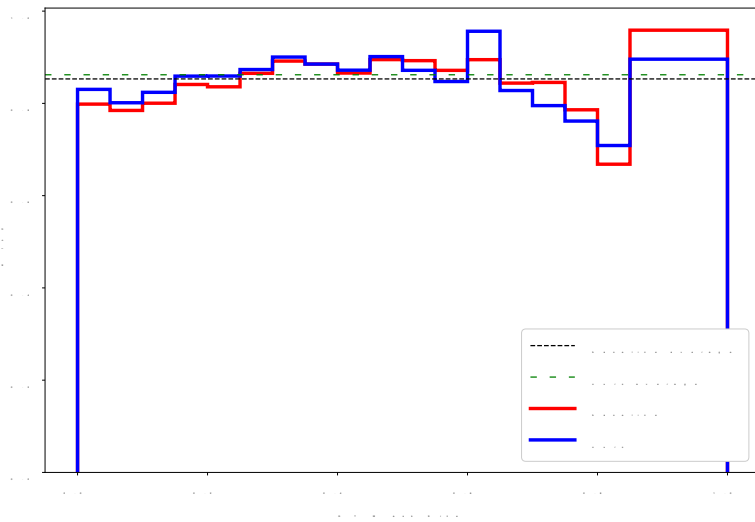


Fig. 8: Distribution of intersection over union to the GT mask size on ECSSD [27].

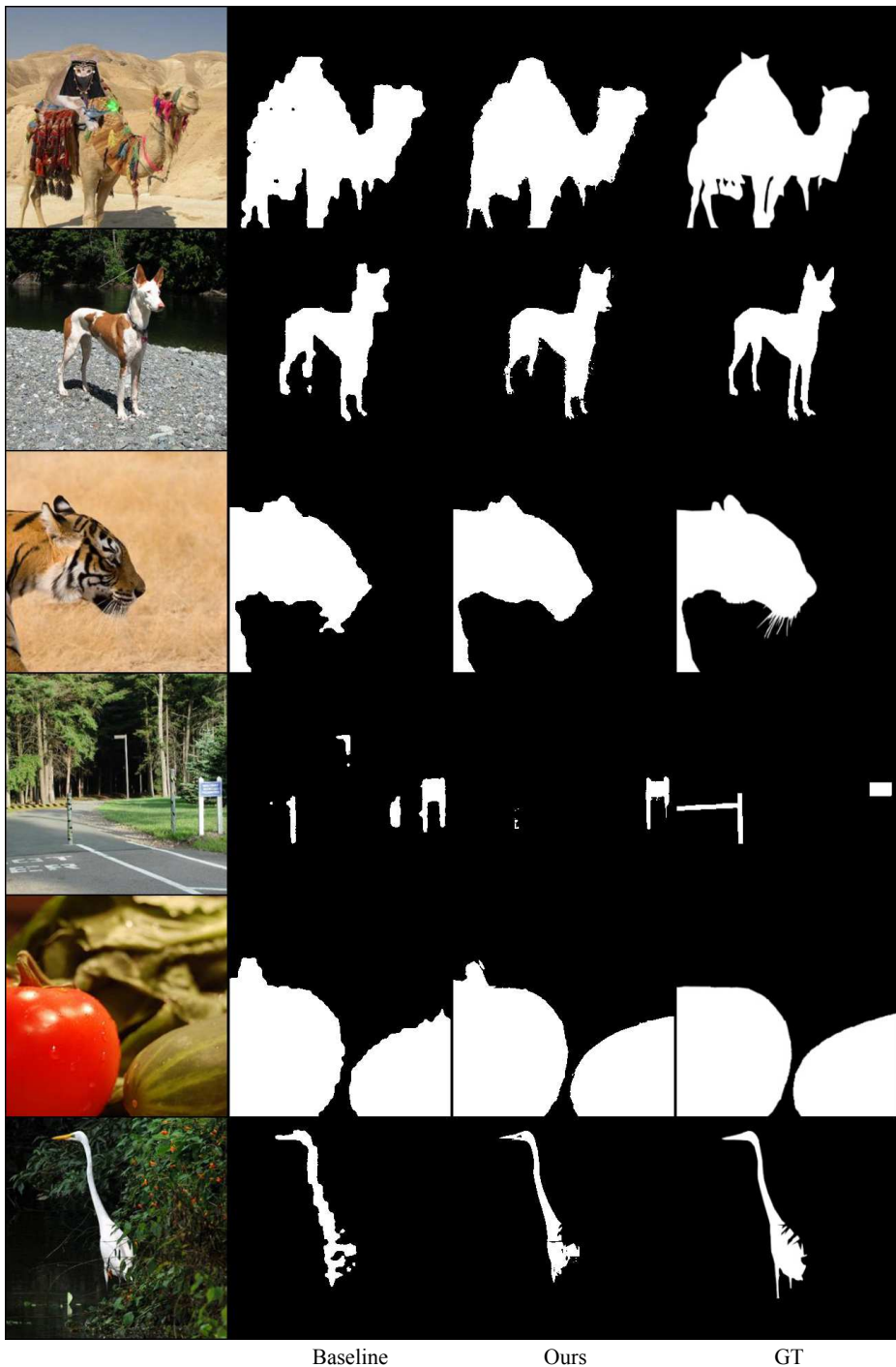


Fig. 9: Quantitative comparison between the baseline and our improved version on random samples from DUTS-TE [33]

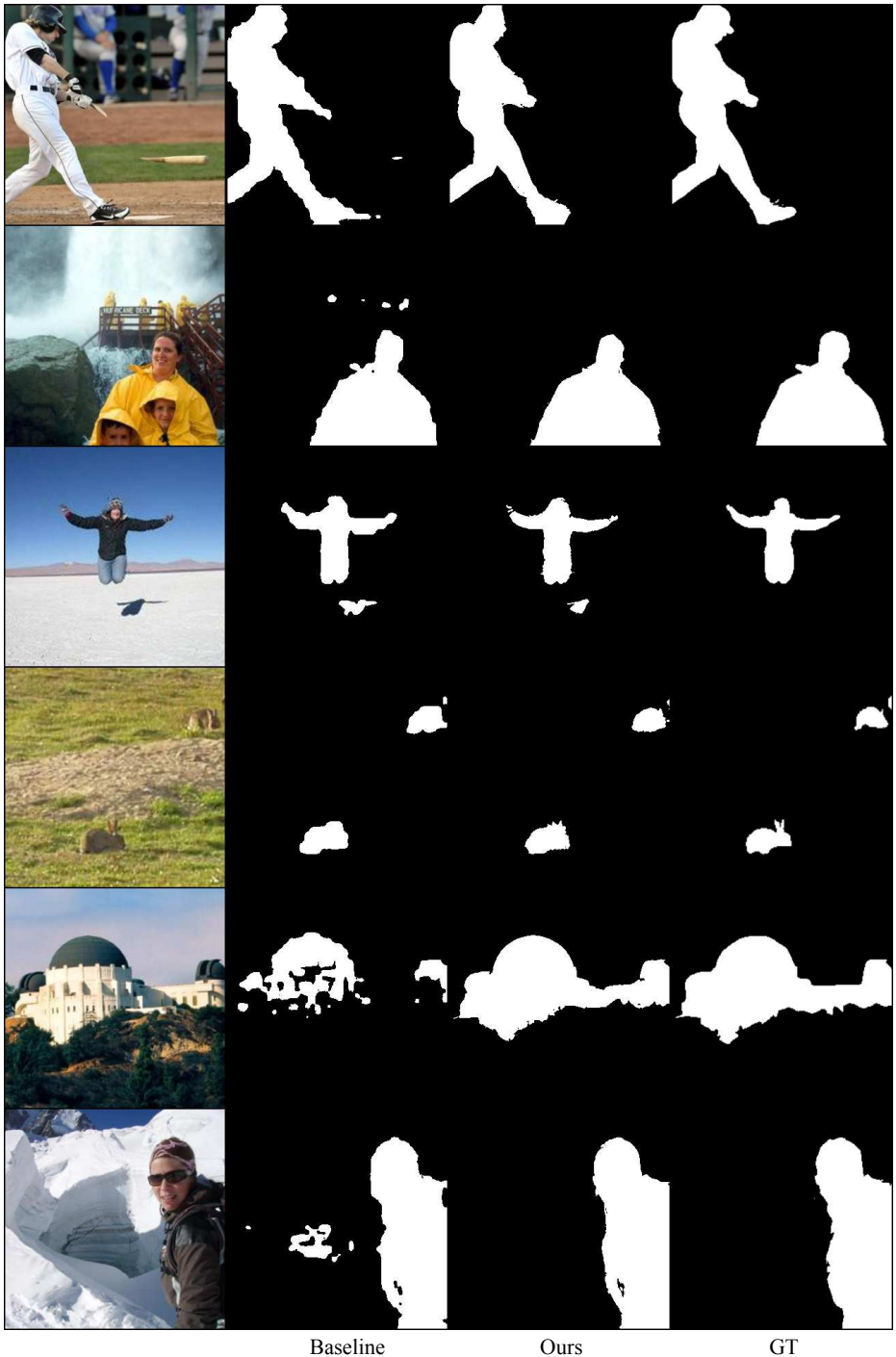


Fig. 10: Quantitative comparison between the baseline and our improved version on random samples from DUT-OMRON [36]

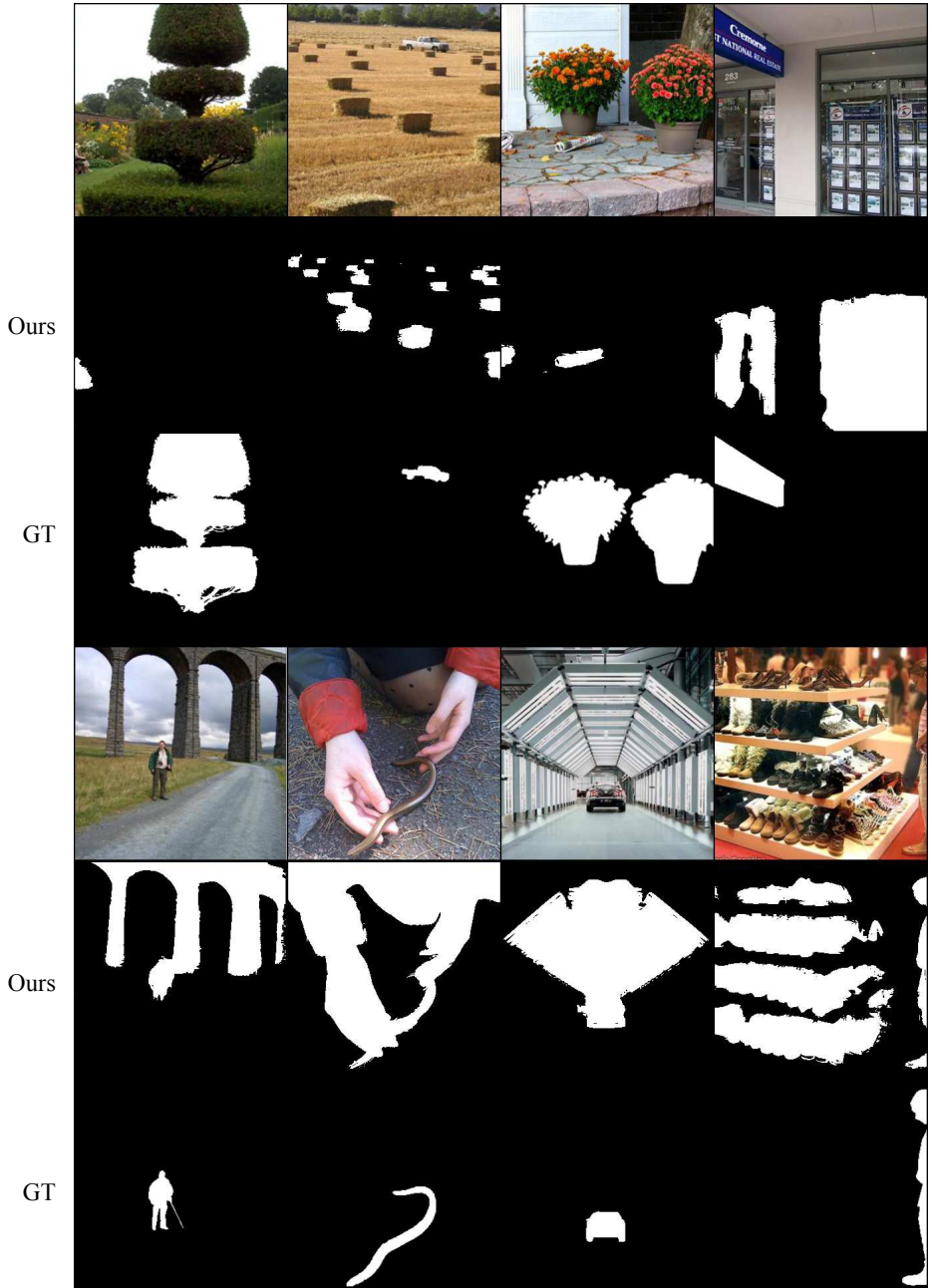


Fig. 11: Failure cases from DUTS-TE [33]